



A model to predict deflection of bevel-tipped active needle advancing in soft tissue



Naresh V. Datla^a, Bardia Konh^a, Mohammad Honarvar^a, Tarun K. Podder^b, Adam P. Dicker^c, Yan Yu^c, Parsaoran Hutapea^{a,*}

^a Department of Mechanical Engineering, Temple University, 1947 North 12th Street, Philadelphia, PA 19122, United States

^b Department of Radiation Oncology, University Hospitals, Case Western Reserve University, Cleveland, OH 44106, United States

^c Department of Radiation Oncology, Thomas Jefferson University, 111 South 11th Street, Philadelphia, PA 19107, United States

ARTICLE INFO

Article history:

Received 25 July 2013

Received in revised form 24 October 2013

Accepted 7 November 2013

Keywords:

Active needle

Flexible needle steering

Tissue–needle interactions

Actuation force

Needle deflection

Energy-based model

ABSTRACT

Active needles are recently being developed to improve steerability and placement accuracy for various medical applications. These active needles can bend during insertion by actuators attached to their bodies. The bending of active needles enables them to be steered away from the critical organs on the way to target and accurately reach target locations previously unachievable with conventional rigid needles. These active needles combined with an asymmetric bevel-tip can further improve their steerability. To optimize the design and to develop accurate path planning and control algorithms, there is a need to develop a tissue–needle interaction model. This work presents an energy-based model that predicts needle deflection of active bevel-tipped needles when inserted into the tissue. This current model was based on an existing energy-based model for bevel-tipped needles, to which work of actuation was included in calculating the system energy. The developed model was validated with needle insertion experiments with a phantom material. The model predicts needle deflection reasonably for higher diameter needles (11.6% error), whereas largest error was observed for the smallest needle diameter (24.7% error).

© 2013 IPEM. Published by Elsevier Ltd. All rights reserved.

1. Introduction

Needle insertion is a percutaneous and minimally invasive technique that is commonly used in medical diagnosis (e.g. biopsy) and treatment (e.g. brachytherapy) procedures. The success of these procedures depends on the accuracy of needle placement at target locations, as well as the ability of the needle to navigate within the tissue to avoid critical organs and to conform the organ shape [1]. To improve the success of the procedures recently there is an increased interest to design active or self-actuating needles that can bend with the help of actuators [1–4].

Hutapea and co-workers [1,2] proposed a smart needle, see Fig. 1, where the cannula was bent by Nitinol wires attached to the body. These Nitinol wires contract when resistively heated beyond a transformation temperature thereby applying bending forces. Similarly, using Nitinol wires as actuators, Ryu et al. [3] developed a prototype of a magnetic resonance compatible active needle. They increased the temperature of Nitinol wires by optical heating. Ayvali et al. [4] developed a prototype of a discretely actuated steerable cannula, where bending forces were achieved by a Nitinol wire that was initially straight at room temperature

and was transformed to a curved configuration when resistively heated. Shape memory alloy is preferred as actuators because of its high power to volume ratio which is critical in surgical needles to minimize the needle size. However, though manageable, a limitation of Nitinol is the relatively high transformation temperature required for actuation that might locally induce thermal damage to surrounding tissue [2]. Alternatively, Webster et al. [5] proposed to steer the needle using pre-curved concentric tubes. This concept was initially implemented with a single active cannula [6] and recently was extended to a multiple active cannula [7]. Several interventions could benefit from these curved needles, such as dosimetric benefits for prostate brachytherapy with active needles [1] and benefits to neurosurgery with the concentric tubes [8].

The maneuverability of active needles can be greatly enhanced using an asymmetric bevel-tip. Several studies including [9] showed that the asymmetry at the needle tip naturally bends these needles. To achieve accurate needle trajectory and targeting there is a need to develop planning and control algorithms of active bevel-tipped needles within tissue [10] based on tissue–needle interaction models. Though these models have already been discussed in the literature for needles with forces applied only at the proximal end to steer the needle (passive needles), such models are yet to be developed for active needles.

* Corresponding author. Tel.: +1 215 204 7805; fax: +1 215 204 4956.

E-mail address: hutapea@temple.edu (P. Hutapea).

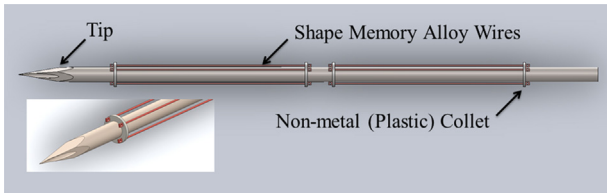


Fig. 1. Schematic of the active surgical needle.

1.1. Related work

Needle insertion with passive needles has been studied both experimentally and numerically which have been summarized by Abolhassani et al. [11] for needle insertion behavior and by Gerwen et al. [12] for needle–tissue interaction forces. Most of the early needle insertion models [13–19] simulated needle insertion without specifically including the tissue–needle interaction forces though experimental work showed the importance of interaction force [20], as pointed out by Misra et al. [21]. However, these interaction forces were considered in the following works [21–26]. Webster [22] developed a nonholonomic kinematic approach to simulate steering of bevel tip needles. Mechanics-based models to predict the needle deflection have also been developed [21,23–26], where tissue–needle interactions are generalized and thereby do not depend on empirical relations developed from previous needle insertion experiments. Kataoka and Washio [23] related the force on the needle to its deflection, while Abolhassani [24] considered the needle deflection as a cantilever beam with a spring support. Misra et al. [21] developed an energy-based model considering classical and fracture mechanics to predict the in-plane bending of bevel tip needles. Roesthuis et al. [25] modified this model to predict in-plane needle deflection with multiple bends by considering tip forces as input and assuming that needle is supported by springs. Later this model was improved by replacing spring support with distributed load [26]. None of the models mentioned above can be applied directly to simulate active needles and therefore have to be modified by including the actuation forces. This paper addresses this issue by presenting a mechanics-based prediction model for deflection of bevel-tipped active needles within soft tissue by incorporating the actuation forces into the model. This mechanics-based tissue–needle model will enable to develop mechanics-based adaptive control algorithms that would be useful for minimizing modeling uncertainties and eliminating surrounding disturbances in real tissue.

An energy-based model has been proposed in this study that was verified with needle-insertion experiments with plastisol gel and bevel-tipped steel needles of 0.38, 0.51, and 0.64 mm diameters. These validation experiments were simplified by replacing shape memory alloy actuation with magnetic forces, which is discussed in greater detail in Section 2.2.1. Finally, comparisons between the predicted and experimentally observed needle tip deflections were made.

2. Methods

2.1. Energy-based model for active needle

An energy-based model was developed to predict the deflection of bevel-tipped active needle during insertion into soft tissue. This model is an extension to the model proposed by Misra et al. [21] for bevel-tipped passive needle. In our model, in addition to the insertion forces, the actuation forces were considered as external forces acting normal to the needle. Considering actuation forces in predicting the deflected shape of the needle enables to improve needle design by helping to optimize actuator size and location, as

well as to plan needle trajectories. Friction forces acting on the needle were not considered because their effect on needle deflection was found to be negligible [21], although they significantly increase the insertion force.

In this model, total system energy is expressed in terms of the transverse, $v(x)$, and axial, $u(x)$, deflections of the needle. Functional forms were initially assumed for needle deflections and then the Rayleigh–Ritz method was used to find the coefficients of these functions. The system energy, Π , was calculated by considering the internal energy stored in the system, U , and the work done by the system, W , as

$$\Pi = U - W \quad (1)$$

The internal energy, U , is composed of the energy stored by needle bending, N_E , and the energy of the tissue deformation, S_E , which are given by

$$N_E = \frac{EI}{2} \int_0^{l_i} \left(\frac{d^2 v_{i-1}}{dx^2} \right)^2 dx + \frac{EI}{2} \int_0^{l_i} \left(\frac{d^2 (v_i - v_{i-1})}{dx^2} \right)^2 dx + \frac{EA}{2} \int_0^{l_i} \left(\frac{du_{i-1}}{dx} \right)^2 dx + \frac{EA}{2} \int_0^{l_i} \left(\frac{d(u_i - u_{i-1})}{dx} \right)^2 dx \quad (2)$$

$$S_E = \frac{1}{2} \int_0^{l_i} K_T (v_i - v_{i-1})^2 dx + \frac{E_T (A l_i)^2}{3(1 - 2\nu_T)} \quad (3)$$

where, subscripts i and $i - 1$ refer to present and previous iterations. E , I , A , and l are the elastic modulus, moment of inertia, cross-section area and length of the needle, respectively. K_T and ν_T are the stiffness and Poisson's ratio of the tissue. Here, N_E is composed of energy due to both transverse and axial deformation of the needle, which are further divided into energy associated in previous step and the incremental increase in energy from previous to current step. Similarly, S_E is composed of axial and transverse deformation of the tissue. Works done on the system include the work of insertion, $W_{insertion}$, and the work of actuation, $W_{actuation}$, expressed as

$$W_{insertion} = P_{insertion} u_i(0) \quad (4)$$

$$W_{actuator} = P_{actuator}^n (v_i(x_m) - v_{i-1}(x_m)) + P_{actuator}^a (u_i(x_m) - u_{i-1}(x_m)) \quad (5)$$

where $P_{insertion}$ is the insertion force. $P_{actuator}^n$ and $P_{actuator}^a$ are the normal and axial actuator forces acting at location x_m of the needle. The needle-tip reaction force R_i , shown in Fig. 2, is resolved into

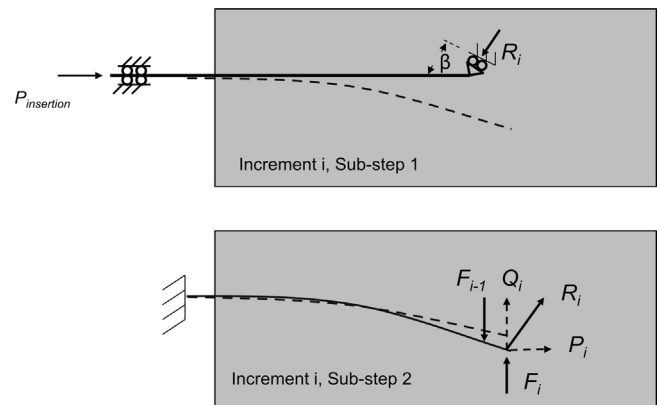


Fig. 2. Illustration showing the forces and boundary conditions acting on the needle in sub-steps 1 and 2 of increment i . R_i , Q_i , and P_i are the reaction force at needle tip and its transverse and axial components, respectively. F_i and F_{i-1} are the actuation forces acting in the current and previous steps.

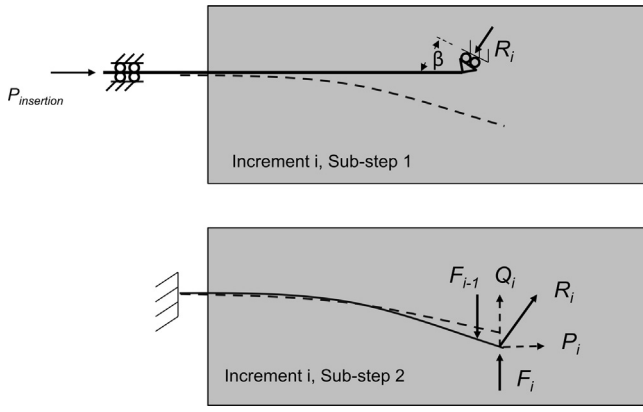


Fig. 2. Illustration showing the forces and boundary conditions acting on the needle in sub-steps 1 and 2 of increment i . R_i , Q_i , and P_i are the reaction force at needle tip and its traverse and axial components, respectively. F_i and F_{i-1} are the actuation forces acting in the current and previous steps.

transverse, Q_i , and axial, P_i components. The work done by these components are given as

$$W_Q = Q_i(v_i(l_i) - v_{i-1}(l_i)) \quad (6)$$

$$W_P = P_i(u_i(l_i) - u_{i-1}(l_i)) \quad (7)$$

where W_Q and W_P are the work done by reaction forces Q_i and P_i , respectively. Also the work which is done in rupturing the tissue, W_R , is

$$W_R = aG_c u_i(l_i) \quad (8)$$

which is a product of the rupture toughness G_c , rupture width a , and rupture length $u_i(l_i)$.

An incremental approach was followed to estimate the needle deflection. In each increment, insertion and actuation forces were

applied on the needle to find the consequent needle deflection and needle advancement in the tissue. Within each increment, two sub-steps were considered as suggested by [21,27], see Fig. 2. In sub-step 1, only insertion force was applied at the proximal end of the needle resulting in reaction forces at the needle tip due to the asymmetry of the needle tip. Then in sub-step 2, these reaction forces along with the actuation forces were applied to the needle resulting in the tissue rupture and the needle deflection. Therefore, in sub-step 1 the work done by the system consists of only $W_{insertion}$, while in sub-step 2 the work done by the system includes W_Q , W_P , $W_{actuator}$, and W_R . The system energies in sub-step 1 and 2 can be expressed as

$$\pi_1 = (N_{E1} + S_{E1}) - W_{insertion} \quad (9)$$

$$\pi_2 = (N_{E2} + S_{E2}) - (W_Q + W_P + W_R + W_{actuator}) \quad (10)$$

The shape functions used in this work are the standard Hermite polynomials for transverse deflection and the linear function for axial deflection, similar to the functions used for passive needles by Misra et al. [21]:

$$v_i = \begin{cases} a_0 + a_1x + a_2x^2 + a_3x^3 & 0 < x \leq \frac{l_i}{2} \\ b_0 + b_1x + b_2x^2 + b_3x^3 & \frac{l_i}{2} < x \leq l_i \end{cases} \quad (11)$$

$$u_i = c_0 + c_1x \quad (12)$$

The geometric boundary conditions applied to these displacement functions for sub-step 1 are

$$v_i(0) = 0, \quad \frac{dv_i(0)}{dx} = 0 \quad \text{and} \quad v_i(l_i) = u_i(l_i) \tan(\beta + \varphi_i) \quad (13)$$

where β is the cut angle defined as the angle between the needle and the cut path, which was assumed to be constant in this study. φ_i

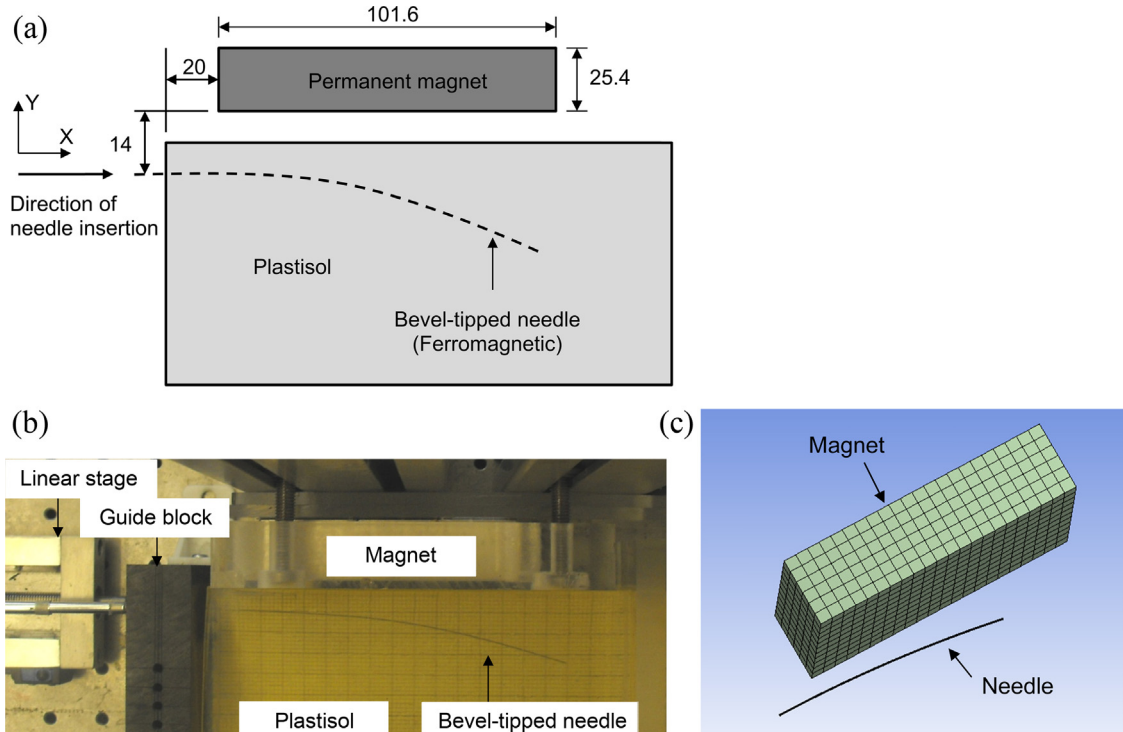


Fig. 3. (a) Schematic, (b) experimental setup, and (c) FE model of the needle insertion setup with the magnet. Actuation (magnetic) forces are applied to the ferromagnetic needle by placing it in the vicinity of a permanent magnet. In (c), the gel around the needle was omitted for clarity. All dimensions in mm, not to scale.

is the slope of the needle at the needle-tip. The boundary conditions for sub-step 2 are

$$v_i(0) = 0, \quad \frac{dv_i(0)}{dx} = 0 \quad \text{and} \quad u_i(0) = 0 \quad (14)$$

2.2. Validation experiment and methods to determine the model parameters

2.2.1. Needle insertion experimental setup

Fig. 3 shows the needle insertion setup used to validate the developed model. The phantom material used for these studies was Plastisol (M-F Manufacturing Co., Ft. Worth, TX, USA), where the elastic modulus of the phantom can be tuned by changing the compositions of plastic (polyvinylchloride suspension) and softener. For example, Misra et al. [21] used plastisol in their needle insertion experiments, where they showed that changing the volume ratio of plastic to softener from 3:1 to 8:1 changed elastic modulus from 22.29 to 45.24 kPa. In this study, plastisol was prepared with 3:1 ratio of plastic to softener. Insertion tests were done with bevel-tipped needles made of spring steel (or piano wire) having bevel angles of 29.25°, 32.73°, and 32.04° for needle diameters of 0.38 mm, 0.51 mm, and 0.64 mm, respectively. A sharp bevel-tip free of burrs was achieved by embedding the spring steel wire at an angle in Crystalbond™ (Aremco Products, Inc., Valley Cottage, NY, USA) mounting adhesive followed by polishing the assembly. After polishing, the needle was removed from the adhesive and then cleaned with Crystalbond™ stripper. These needles were inserted into the plastisol gel at a constant speed of 2.5 mm/s by attaching the needle to a motorized linear stage (Velmex Inc., Bloomfield, NY, USA) of 6 µm resolution.

These validation experiments were simplified by replacing actuation forces from shape memory alloy (as proposed in [1–4]) with magnetic forces. It should be noted that the magnetic forces are not proposed to actuate the real surgical needle, but are being used here only to simulate the actuation forces of the shape memory alloy actuators. Moreover, the use of magnetic forces to understand active needle behavior will help to expedite the development of Nitinol actuated needles. The use of magnetic forces simplifies the model by eliminating the geometric complexities such as the protruding actuator attached to the needle body and its consequent effect on needle stiffness and insertion forces. The model can be modified in future to account for Nitinol actuator by correcting the stiffness of the needles and considering the additional energy needed to rupture tissue. It should be noted that these modifications could be done once the dimensions and mechanical properties of the actuator are known. With these refinements, the model can be used to assess the needle–tissue interactions of various needle designs and thereby lead to improved active needle design.

The magnetic (or actuation) forces were applied to the needle by placing a Neodymium permanent magnet in the vicinity of the needle (piano wire). Since piano wire is ferromagnetic, the permanent magnet applies transverse forces on the needle and therefore affects the deflection of needle. These external magnetic forces help to bend the needle similar to the effect of actuation forces on the active needle deflection (like in Fig. 1). The permanent magnet used was a grade N42 rectangular block of 101.6 mm long × 50.8 mm wide × 25.4 mm thick, magnetized through the thickness. Out-of-plane magnetic forces were eliminated by placing the magnet such that the mid-width of the magnet was in the plane of needle bending. This magnet was placed 20 mm from the point of needle insertion in the direction of insertion and at a 14 mm offset distance in the normal direction to straight needle, as shown in Fig. 3(a). The magnet was secured by being enclosed in a rigid polycarbonate plastic and attaching the assembly to a rigid aluminum bracket. It should be noted that the materials chosen for fasteners

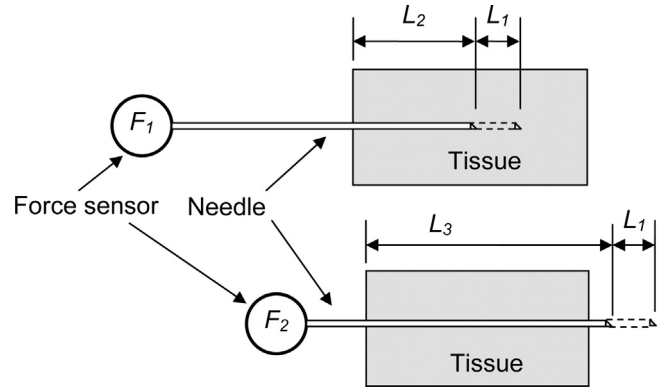


Fig. 4. Rupture toughness of the tissue was determined from the needle insertion forces measured during rupture (needle tip within tissue, F_1) and after rupture (needle tip pass other end of tissue, F_2).

are non-magnetic to minimize interfere with the magnetic fields between the magnet and the needle.

Passive needles were inserted at an offset distance varying between 50 and 70 mm, where offset distance is the transverse distance between the line of action of needle insertion and tissue boundary. For active needles, the chosen offset of 14 mm (shown in Fig. 2) was optimized to maximize the actuation (or magnetic) forces by being closer to magnet, as well as to minimize the boundary constraints by not being too close to the phantom boundary. This assumption on boundary constrain effect was verified by repeating passive needle insertion with 0.51 mm needle for offsets of 14 and 50 mm. Despite the changes in offset distances the needle-tip deflections differed by 4.5% (28.2 mm and 27.0 mm deflections for 14 mm and 50 mm offsets, respectively), thereby showing negligible effects of offset and boundary constraints.

2.2.2. Plastisol elasticity and toughness measurements

Elastic modulus was determined by indentation tests performed under displacement control using a custom built load frame. Indentation was done normal to the surface of plastisol, which was unconstrained. A spherical indenter of 10 mm diameter was loaded normally into the sample to a depth of 4 mm at a speed of 1 mm/s followed by immediately unloading to the initial position at the same speed. Prior to indentation, the instant of initial contact was determined by observing the change in indentation force when the indenter was advanced in increments of 40 µm. Using the Oliver–Pharr method [28] the elastic modulus was calculated from the slope of fourth degree polynomial fit to the load-indentation depth curve, at the beginning of the unloading curve.

Rupture toughness was determined from the insertion force measured during needle insertion into the phantom, similar to Azar and Hayward [29] and Misra et al. [21]. To determine the rupture toughness, the depth of needle insertion was chosen to be longer than the length of sample. As shown in Fig. 4, there are two stages of insertion: (a) while the needle tip is within the tissue that involves tissue rupture, and (b) while a part of the needle is within tissue and the needle tip passes beyond the other end of the tissue. Insertion force in the first phase, F_1 , is a combination of rupture and friction forces; whereas the insertion force in the second phase, F_2 , comprises only the friction force. The work done during the first phase for cutting and friction (G_1) and for friction alone (G_2) are given as

$$G_1 = \int_{L_2}^{L_2+L_1} F_1 dL \quad (15)$$

$$G_2 = \int_{L_3}^{L_3+L_1} \left(\frac{L_2 + (L_1/2)}{L} \right) F_2 dL \quad (16)$$

the needle length before the first and second phases, respectively. G_2 was normalized to the average needle length $(L_2 + L_1/2)$ in the first phase. The work done in rupture or rupture toughness, G_c , is given by [21]

$$G_c = \frac{1}{A}(G_1 - G_2) \quad (17)$$

where A is the fracture area created.

2.2.3. Finite element (FE) model to estimate magnetic forces on needle

Fig. 3(c) shows the 3D FE model developed using ANSYS 14.5 (Ansys Inc., Canonsburg, PA). The magnetic forces were determined from the model using the magnetostatic analysis capability of ANSYS. In addition to modeling the magnet and needle, a rectangular enclosure was modeled around the magnet and needle that spans 50 mm in each direction. This enclosure was modeled as a material with relative permittivity of air ($\mu_r \approx 1$) based on the assumption that the phantom used was unsusceptible to magnetic field. To verify this assumption magnetic flux was measured with a gaussmeter that was placed at a distance from the magnet and separated from the magnet with either air or phantom. Negligible changes in magnetic flux with both air and phantom validated the assumption that the enclosure can be modeled as air. The 20-node SOLID117 elements were used for the needle, magnet and enclosure. The needle was modeled as having a constant radius of curvature (R) that was determined from the experimentally observed shape of the deflected needle after 150 mm insertion into the plastisol gel in the presence of the magnet. This value of R value was determined by fitting a circle of radius R to the starting and ending points of the deflected needle. Multiple simulations were done with different insertion depths, where in each case the length of the needle modeled was same as the insertion depth. The magnet's external Gauss strength and coercivity used were 13.2 kG and 935 kA/m, respectively, which were provided by the manufacturer.

3. Results and discussion

3.1. Needle insertion experiments

Fig. 5 shows the tip deflection of bevel-tip needles of 0.38, 0.51, and 0.64 mm diameters inserted into the plastisol gel to a depth of 150 mm at a rate of 2.5 mm/s. It can be seen that, as expected, with passive needles the amount of needle tip deflection decreases (or curvature increases) as needle diameter increases, similar to the trend observed in [30] with Nitinol needles. Considering that the three needles have similar bevel angles, increase in the needle diameter increases the needle stiffness that increasingly resists

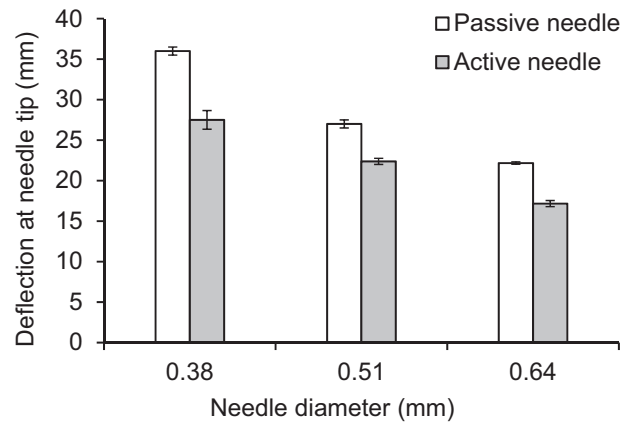


Fig. 5. Needle tip deflections measured without and with actuation (magnetic) forces for different needle diameters.

needle deflection thereby resulting in decrease in needle deflection. More importantly, Fig. 5 shows that for all needle diameters the needle deflection was smaller in active needles than in passive needles. This is also expected as the bevel tip was oriented such that needle moves away from the magnet ($-y$ -axis of Fig. 3(a)), whereas the magnetic forces attract the needle toward the magnet ($+y$ -axis of Fig. 3(a)). In other words, the magnetic forces and bevel-tip forces act in opposite directions and thereby decrease the total effective force acting on the needle tip which consequently decreases the amount of needle deflection in the active needle. It should be noted that by reversing the needle orientation in Fig. 3(a) the needle deflection would be higher in active needles than in passive needles, because both magnetic forces and bevel-tip forces will then act in the same direction. Trails by reversing the bevel orientation showed negligible increase in needle deflection because the offset distance between the needle and magnet had to be increased (to accommodate the needle moving toward the magnet) that resulted in negligible magnetic (or actuation) forces.

3.2. Plastisol elasticity and toughness measurements

The elastic modulus determined from the measured indentation forces (see Fig. 6(a)) was 25.6 ± 0.6 kPa, which was close to the modulus value of 22.29 kPa determined for similar plastisol gel in Ref. [21]. Therefore, in this study we used the tissue stiffness K_T of 4.83 kN/m² that was determined in their work. The choice of the plastisol gel used in this study is justified by the close match in the elastic modulus of biological tissues such as prostate tissue, which was 24.1 ± 14.5 kPa for cancerous tissue and 17.0 ± 9.0 kPa for healthy tissue [31]. Fig. 6(b) shows a representative insertion

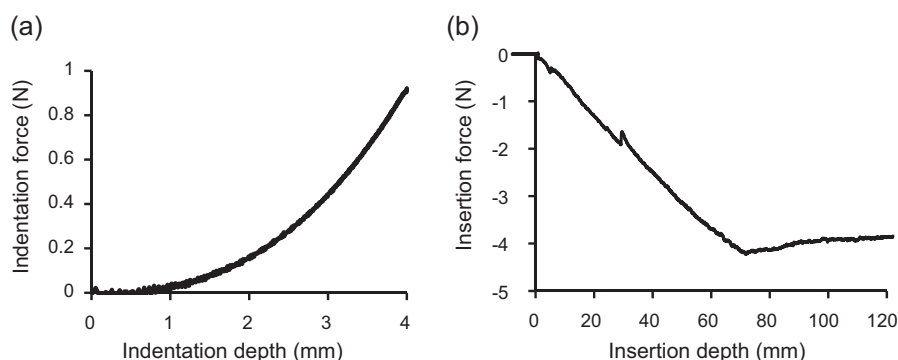


Fig. 6. (a) Indentation force measured for plastisol gel. (b) Insertion force measured when the 0.64 mm spring steel bevel-tip needle was inserted at a constant rate of 2.5 mm/s. The insertion force reached a plateau, about 75 mm, after the needle tip passed the other end of the phantom.

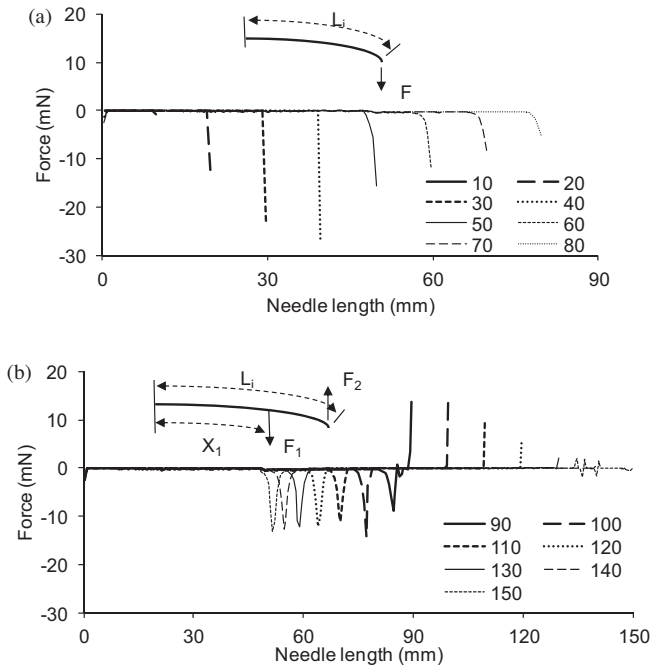


Fig. 7. FE predicted normal force distribution along length of the 0.38 mm diameter needle. Force distribution is different for insertion depth (a) below and (b) above 90 mm. The schematic within the plot show the equivalent point loads acting on the needle when the magnet is placed in the +y-axis relative to the needle, therefore F and F_1 are attractive magnetic forces and F_2 is repulsive magnetic force.

force measured when bevel-tip needles of 0.64 mm diameter was inserted into a plastisol gel of about 70 mm length at insertion speed of 2.5 mm/s. It can be seen that in the first stage as insertion depth increased the insertion force increased. This trend is expected because as insertion depth increases the contact surface between the tissues and needle increase that consequently increases the friction forces. After the needle tip passes beyond the other end

of the sample (about 70 mm), the insertion force initially relaxes and then reaches a plateau because the contact area to needle and thereby friction forces remains unchanged. The rupture toughness determined using Eq. (17) was 143.4 N/m.

3.3. FE estimated actuation (magnetic) forces

The applied magnetic forces on the needle during insertion were determined using the FE model shown in Fig. 3(c). Fig. 7 shows a representative magnetic force distribution along needle length at various insertion depths for a 0.38 mm diameter needle. It can be seen that force distribution follows two distinct stages: (i) for insertion depth less than 90 mm a peak force acts at the needle tip: a pull force (F) acts about the needle tip while negligible forces act on the rest of the needle length, and (ii) for insertion depths 90 mm and above two peak forces act on the needle: a repulsive force (F_2) acts about the needle tip and a pull force (F_1) acts at a distance X_1 from distal end of the needle. These two distinct stages are due to the nature of the magnetic field around the magnet. To simplify the analytical model, the peak load distributions were replaced with point loads acting normal to the needle. The magnitude of these point loads was calculated using the moment equilibrium about the distal end of the needle. Fig. 8 shows the summary of the point loads (F , F_1 , and F_2) and the location of peak load (X_1) for the three needle diameters. The variation of these forces and location with insertion depth were fit to cubic and linear polynomials, as shown in Fig. 8. The magnetic forces and location estimated with these polynomials were input as actuation loads to the analytical model. It can be seen from Fig. 8 that, for all three diameters, as insertion depth increased F increased initially and then reached an approximately constant value, F_1 was approximately constant while its location (X_1) moved closer to the distal end of the needle, and F_2 decreased. The work done by actuation forces, given by Eq. (5), will be modified accordingly for stages 1 and 2 as follows:

$$W_{actuator}^1 = F(l_i)(v_i(l_i) - v_{i-1}(l_i)) \quad (18)$$

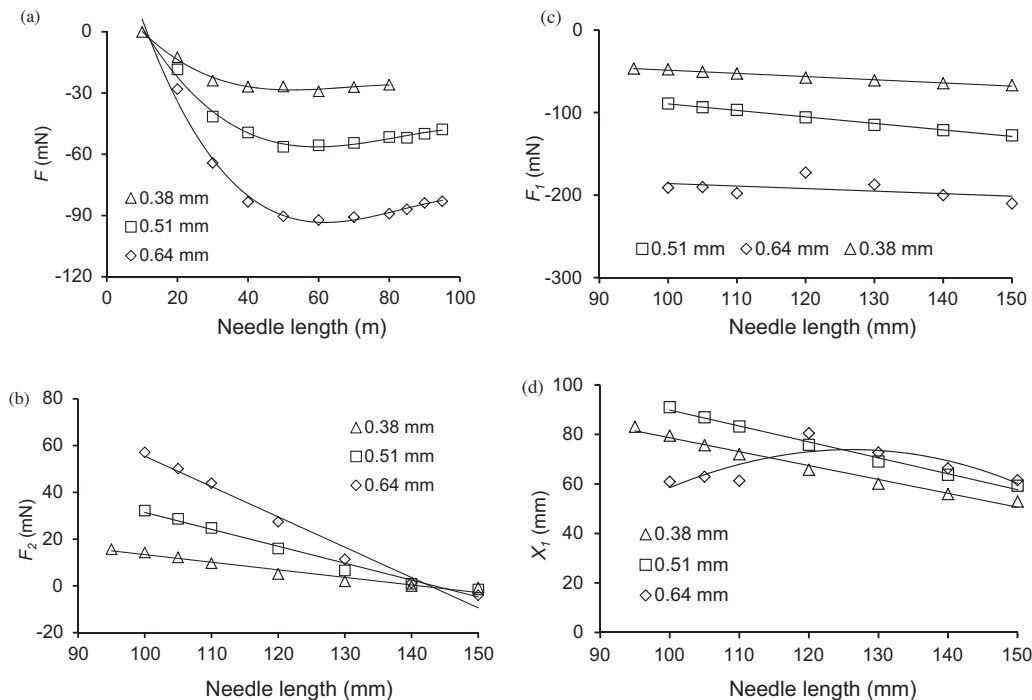


Fig. 8. Equivalent FE estimated magnetic forces and location (a) F , (b) F_2 , (c) F_1 , and (d) X_1 at different insertion depths. These equivalent forces were determined from the force distributions shown in Fig. 7. The curves are the cubic and linear curve fits to the data.

Table 1

Comparison of the needle tip deflections between experiments and model for different needle diameters. Standard deviation values are given for experimental data done with three repetitions.

Diameter (mm)	$P_{insertion}$ (mN)	Needle tip deflection (mm)					
		Passive needle			Active needle		
		Experiment	Model	% Error	Experiment	Model	% Error
0.38	10	36.0 ± 1.0	37.8	–5.0	27.5 ± 2.3	20.7	24.7
0.51	15	27.0 ± 1.0	28.5	–5.5	22.4 ± 0.7	19.8	11.6
0.64	22	22.2 ± 0.3	22.3	–0.5	17.2 ± 0.8	19.2	–11.6

$$W_{actuator}^2 = F_1(l_i)(v_i(X_{1_i}) - v_{i-1}(X_{1_i})) + F_2(l_i)(v_i(l_i) - v_{i-1}(l_i)) \quad (19)$$

where $W_{actuator}^1$ and $W_{actuator}^2$ are the actuation work for stages 1 and 2, respectively. It should be noted that the axial component of the actuator forces are neglected in Eqs. (18) and (19) because they were found to be negligible; i.e. the FE model showed that the axial magnetic forces are at most 10% of the normal forces and thus have negligible effect on needle bending.

The FE estimated magnetic forces were validated with a simple needle bending experiments in air. In this experiment, initially,

needle deflection in air due to magnetic forces was measured by placing a piano wire (0.51 mm diameter, 125 mm long) in air at a offset distance of 60 mm away from the magnet (similar to Fig. 3 except that phantom was replaced with air). The measured deflection of the needle tip was 9 mm. Then using the FE model with the deflected needle shape the magnetic force distribution on the needle was determined to be in the second stage ($F_1 = 15.1$ mN, $X_1 = 103.9$ mm, and $F_2 = 3.8$ mN). Finally, these estimated forces combined with beam theory were used to estimate the deflection of the needle, which was then compared to the experimentally observed needle deflection. The experimentally observed and estimated deflections differed by 12.5% (9.0 mm and 7.9 mm, respectively). Considering variability in the properties of magnet obtained from the manufacturer and subsequently used in the FE model, the FE model reasonably predicted the magnetic forces.

3.4. Comparison between the model and experiments

Numerical simulations were first done with passive needle (without magnetic forces) to solve for the coefficients in displacement functions, in Eqs. (11) and (12), by applying the Rayleigh–Ritz method to Eqs. (9) and (10). The elastic modulus of the spring steel needle and plastisol gel were 190 GPa and 22.29 kPa, respectively. The simulation parameters required to determine the needle deflection are the insertion force ($P_{insertion}$) and cut angle (β), which were optimized to minimize the differences in measured and estimated needle tip deflections. The determined $P_{insertion}$ values were 10 mN, 15 mN, and 22 mN for needle diameters of 0.38 mm, 0.51 mm, and 0.64 mm, respectively, and the β value was 0.75. Table 1 shows that for passive needles negligible differences exist for needle tip deflections between experiment and model, maximum error in prediction being 5.5%.

Simulations for active needle were done with $P_{insertion}$ and β values used for the passive needle. The actuation work was calculated using Eqs. (18) and (19), where F , F_1 , F_2 and X_1 values were determined using the polynomials fits shown in Fig. 8. Fig. 9 shows the needles shapes predicted for passive and active needles. Table 1 shows the comparison of the needle tip deflections between simulation and experiment. It can be seen that the model reasonably predicts needle deflection for higher needle diameters (maximum prediction error was 11.6% for 0.51 and 0.64 mm needles), whereas the largest error was observed for the smallest needle diameter (prediction error of 24.7% for 0.38 mm needle). Considering several assumptions made to the model such as using a two-dimensional model, approximating the magnetic forces, optimizing the cutting angle and insertion forces, and neglecting the friction forces, the model predicts needle deflection with reasonable accuracy. Moreover, these prediction errors fall in the same range as the errors reported by Misra et al. [21] with their energy-based model on which our model was developed.

The developed model can be used to improve the design of active needle to achieve greater steerability. For example, this model can be used to achieve a specified deflection by selecting suitable actuation forces and by optimizing the actuator location. This has been illustrated in Fig. 10 with 0.38 mm diameter needle that shows the

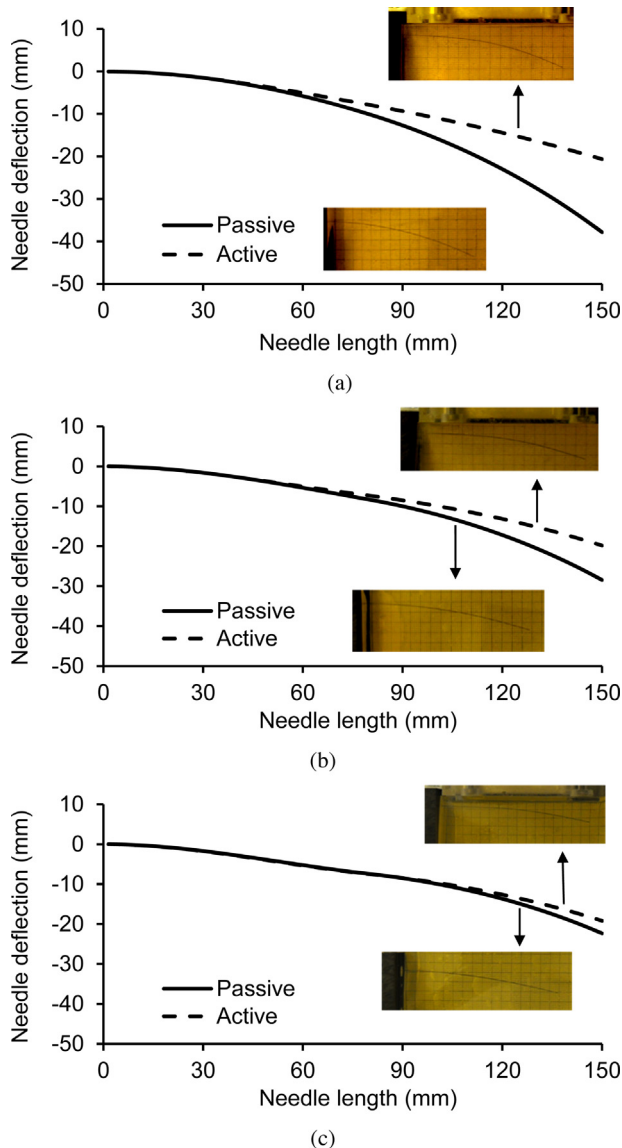


Fig. 9. Simulated deflected shape of passive and active needles of (a) 0.38 mm, (b) 0.51 mm, and (c) 0.64 mm diameters inserted 150 mm into plastisol gel. The images in plot show the experimentally observed needle deflection after 150 mm insertion.

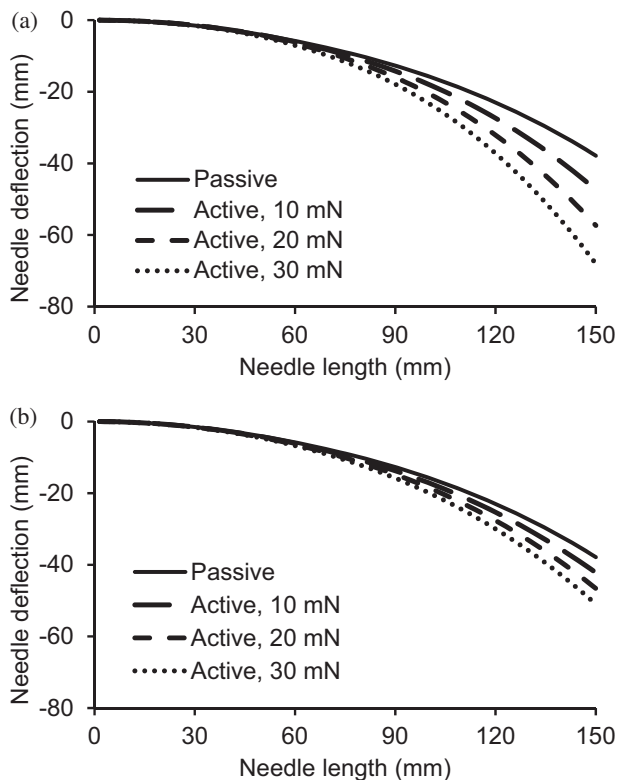


Fig. 10. Simulated deflected shape of 0.38 mm diameter needle inserted 150 mm into phantom with actuation forces acting at (a) needle tip and (b) 10 mm away from needle tip. These forces act normal to the needle in the direction of the bevel orientation. The force values are given in legend.

effects of actuator location and force on needle-tip deflection. It can be seen in both Figs. 10(a) and (b) that as expected increasing the actuation force moves the needle away from the deflected shape of the passive needle. Moreover, the needle deflection is higher in active needles than in passive needle because both actuation force and bevel-tip forces act in the same direction. More importantly, it is observed that the needle deflection was maximum when actuation forces are applied at needle tip, Fig. 10(a), rather than away from the tip, Fig. 10(b). For example, moving an actuation force of 10 mN from needle tip to 10 mm away from needle tip decreased needle-tip deflection from 47.4 to 42.2 mm.

4. Conclusions

An energy-based model was presented to predict the needle deflection of active bevel-tipped needles. In this model actuation forces were added to a previously existing model for passive needles. This model was verified with needle-insertion experiments with plastisol gel and bevel-tipped spring steel (ferromagnetic) needles of 0.38, 0.51, and 0.64 mm diameters. Actuation forces were applied to the needle by placing a permanent magnet in the vicinity of the ferromagnetic needle. These magnetic forces were determined by magneto-static analysis using a finite element model. The determined actuation (magnetic) forces were input to the model along with geometric and mechanical properties of needle and plastisol gel to predict the needle deflection within plastisol gel. Comparison of the model prediction with experimental results showed reasonable prediction accuracy.

Funding

None.

Ethical approval

Not required.

Acknowledgments

This work is supported by the Department of Defense CDMRP Prostate Cancer Research Program (Grant# W81XWH-11-1-0397/98/99).

Conflict of interest statement

None declared.

References

- [1] Podder TK, Dicker AP, Hutapea P, Darvish K, Yu Y. A novel curvilinear approach for prostate seed implantation. *Med Phys* 2012;39:1887–92.
- [2] Datla NV, Konh B, Koo JJY, Choi DJW, Yu Y, Dicker AP, et al. Polyacrylamide phantom for self actuating needle–tissue interaction studies. *Med Eng Phys* 2013. <http://dx.doi.org/10.1016/j.medengphy.2013.07.004> (in press).
- [3] Ryu SC, Renaud P, Black RJ, Daniel BL, Cutkosky MR. Feasibility study of an optically actuated MR-compatible active needle. In: 2011 IEEE/RSJ international conference on intelligent robots and systems. 2011. p. 2564–9.
- [4] Ayvali E, Liang C-P, Ho M, Chen Y, Desai JP. Towards a discretely actuated steerable cannula for diagnostic and therapeutic procedures. *Int J Rob Res* 2012;31:588–603.
- [5] Webster R. Mechanics of precurved-tube continuum robots. *IEEE Trans Robot* 2009;25:67–78.
- [6] Burgner J, Swaney P, Rucker DC, Gilbert HB, Nill ST, Russell PT, et al. A bimanual teleoperated system for endonasal skull base surgery. In: Proceedings of 2011 IEEE/RSJ international conference on intelligent robots and systems. 2011. p. 2517–23.
- [7] Burgner J, Swaney PJ, Lathrop RA, Weaver KD, Webster RJ. Robot-assisted intracerebral hemorrhage evacuation: an experimental evaluation. In: Holmes DR, Yaniv ZR, editors. Proceedings of SPIE medical imaging. 2013. 8671:86710H.
- [8] Anor T, Madsen JR, Dupont P. Algorithms for design of continuum robots using the concentric tubes approach: a neurosurgical example. In: IEEE international conference on robotics and automation. 2011. p. 667–73.
- [9] Engh JA, Podnar G, Kondziolka D, Riviere CN. Toward effective needle steering in brain tissue. *Conf Proc IEEE Eng Med Biol Soc* 2006;1:559–62.
- [10] Ruiz B, Hutapea P, Darvish K, Dicker AP, Yu Y, Podder TK. SMA actuated flexible needle control using EM sensor feedback for prostate brachytherapy. In: IEEE international conference on robotics and automation. 2012.
- [11] Abolhassani N, Patel R, Moallem M. Needle insertion into soft tissue: a survey. *Med Eng Phys* 2007;29:413–31.
- [12] Van Gerwen DJ, Dankelman J, van den Dobbelsteen JJ. Needle-tissue interaction forces – a survey of experimental data. *Med Eng Phys* 2012;34:665–80.
- [13] Alterovitz R, Goldberg K. Needle insertion and radioactive seed implantation in human tissues: simulation and sensitivity analysis. In: Proceedings of IEEE international conference on robotics and automation, vol. 2. 2003. p. 1793–9.
- [14] DiMaio SP, Salcudean SE. Interactive simulation of needle insertion models. *IEEE Trans Biomed Eng* 2005;52:1167–79.
- [15] Nienhuys H-W, van der Stappen AF. A computational technique for interactive needle insertions in 3D nonlinear material. In: Proceedings of 2004 IEEE international conference on robotics and automation, vol. 2. 2004. p. 2061–7.
- [16] Crouch JR, Schneider CM, Wainer J, Okamura AM. A velocity-dependent model for needle insertion in soft tissue. *Med Image Comput Comput Assist Interv* 2005;8(Pt 2):624–32.
- [17] Heverly M, Dupont P, Friedman J. Trajectory optimization for dynamic needle insertion. In: Proceedings of IEEE international conference on robotics and automation. 2005. p. 1658–63.
- [18] Hing JT, Brooks aD, Desai JP. Reality-based needle insertion simulation for haptic feedback in prostate brachytherapy. In: Proceedings of 2006 IEEE international conference on robotics and automation (ICRA). 2006. p. 619–24.
- [19] Yan KG, Podder T, Yu Y, Liu T-I, Cheng CWS, Ng WS. Flexible needle-tissue interaction modeling with depth-varying mean parameter: preliminary study. *IEEE Trans Biomed Eng* 2009;56:255–62.
- [20] Okamura AM, Simone C, O’Leary MD. Force modeling for needle insertion into soft tissue. *IEEE Trans Biomed Eng* 2004;51:1707–16.
- [21] Misra S, Reed KB, Schafer BW, Ramesh KT, Okamura AM. Mechanics of flexible needles robotically steered through soft tissue. *Int J Rob Res* 2010;29:1640–60.
- [22] Webster RJ. Nonholonomic modeling of needle steering. *Int J Rob Res* 2006;25:509–25.
- [23] Kataoka H, Washio T. A model for relations between needle deflection, force, and thickness on needle penetration. In: Medical image computing and computer-assisted intervention; 2001. p. 966–74.
- [24] Abolhassani N, Patel RV. Deflection of a flexible needle during insertion into soft tissue. *Conf Proc IEEE Eng Med Biol Soc* 2006;1:3858–61.

- [25] Roesthuis RJ, van Veen YR, Jahya A, Misra S. Mechanics of needle–tissue interaction. In: 2011 IEEE/RSJ international conference on intelligent robots and systems. 2011. p. 2557–63.
- [26] Roesthuis RJ, Abayazid M, Misra S. Mechanics-based model for predicting in-plane needle deflection with multiple bends. In: 2012 4th IEEE RAS EMBS international conference on biomedical robotics and biomechatronics. 2012. p. 69–74.
- [27] Barbé L, Bayle B, de Mathelin M, Gangi A. Needle insertions modeling: identifiability and limitations. *Biomed Signal Process Control* 2007;2:191–8.
- [28] Oliver WC, Pharr GM. An improved technique for determining hardness and elastic modulus using load and displacement sensing indentation experiments. *J Mater Res* 1992;7:1564–83.
- [29] Azar T, Hayward V. Estimation of the fracture toughness of soft tissue from needle insertion. In: Bello F, Eddie Edwards PJ, editors. *Biomedical simulation*. Berlin, Heidelberg: Springer; 2008. p. 166–75.
- [30] Van Veen YR, Jahya A, Misra S. Macroscopic and microscopic observations of needle insertion into gels. *Proc Inst Mech Eng Part H J Eng Med* 2012;226:441–9.
- [31] Ahn B-M, Kim J, Ian L, Rha K-H, Kim H-J. Mechanical property characterization of prostate cancer using a minimally motorized indenter in an ex vivo indentation experiment. *Urology* 2010;76:1007–11.